Additive Manufacturing 30 (2019) 100842

Contents lists available at ScienceDirect

Additive Manufacturing

journal homepage: www.elsevier.com/locate/addma

Full Length Article

3D printed architected hollow sphere foams with low-frequency phononic band gaps

Olivia McGee[a], Huan Jiang[a], Feng Qian[b], Zian Jia[c], Lifeng Wang[c], Han Meng[d], Dimitrios Chronopoulos[d], Yanyu Chen[a,*], Lei Zuo[b,*]

[a] Department of Mechanical Engineering, University of Louisville, Louisville, KY 40292, USA
[b] Department of Mechanical Engineering, Virginia Tech, Blacksburg, VA 24061, USA
[c] Department of Mechanical Engineering, Stony Brook University, Stony Brook, NY 11794, USA
[d] Institute for Aerospace Technology & The Composites Group, The University of Nottingham, NG7 2RD, UK

ARTICLE INFO

Keywords:
3D printing
Hollow sphere foam
Band gap
Phononic crystals
Noise and vibration

ABSTRACT

We experimentally and numerically investigate elastic wave propagation in a class of lightweight architected materials composed of hollow spheres and binders. Elastic wave transmission tests demonstrate the existence of vibration mitigation capability in the proposed architected foams, which is validated against the numerically predicted phononic band gap. We further describe that the phononic band gap properties can be significantly altered through changing hollow sphere thickness and binder size in the architected foams. Importantly, our results indicate that by increasing the stiffness contrast between hollow spheres and binders, the phononic band gaps are broadened and shifted toward a low-frequency range. At the threshold stiffness contrast of 50, the proposed architected foam requires only a volume fraction of 10.8% while exhibiting an omnidirectional band gap size exceeding 130%. The proposed design paradigm and physical mechanisms are robust and applicable to architected foams with other topologies, thus providing new opportunities to design phononic metamaterials for low-frequency vibration control.

1. Introduction

Noise and vibration are becoming an increasingly hazardous form of pollution as cities become busier and technology advances. Sources of noise and vibration pollution can be airborne or structural-borne and include construction, traffic, and wind. These undesired noises and vibration not only have negative impacts on the physical and social health by impacting sleep patterns, hearing abilities, and concentration [1,2], but also deteriorate the structural integrity of civil infrastructures [3,4] and the functionality of high-precision industrial equipment [5]. To control noise and vibration pollution, both active and passive control methods have been developed in the past few decades. Active noise control works best for mechanical waves that travel primarily in the longitudinal direction through gas mediums, such as air. In this method, a second wave is generated to interactive with the wave source and they ultimately cancel each other out. Though the operating frequency range is limited, the perfect control effect makes this approach have many applications such as noise-canceling headphones, active mufflers, and anti-snoring devices [6,7]. Passive control involves the passing of waves through a soft or hard material so that the mechanical waves will either be dampened or reflected, respectively. Because of the broad vibration control frequency range, the passive approach has been widely employed in pumps, motors, isolation of civil engineering structures, and sensitive laboratory equipment [8–10]. While each method is effective in its own way, these control methods can contribute negatively to the cost or mass of a system and are not appropriate in all applications [11]. Many newly-developed composites such as carbon fiber-reinforced composites exhibit increased strength properties at the expense of noise and vibration control capabilities compared to more traditional soft bulk materials used in passive control approach [12]. For this reason, the architectures and mechanical properties of composite materials are being analyzed and optimized to exhibit enhanced strength and damping properties [13,14].

Moving towards architected materials, which are rationally designed multiscale material systems, exhibit novel functionalities and unique properties that cannot be readily achieved in natural bulk solids [15,16]. In addition to the unusual mechanical and physical properties, architected materials have been designed and optimized for novel elastodynamic wave phenomena. One example of such architected materials is phononic metamaterial, which consists of periodically

* Corresponding authors.
E-mail addresses: yanyu.chen@louisville.edu (Y. Chen), leizuo@vt.edu (L. Zuo).

https://doi.org/10.1016/j.addma.2019.100842
Received 22 July 2019; Received in revised form 29 August 2019; Accepted 2 September 2019
Available online 03 September 2019

topological structures and materials dispersions and has the ability to manipulate the propagation of mechanical waves [17–29]. The periodic structures of phononic crystals produce omnidirectional band gaps-ranges of frequencies where elastic waves cannot propagate. In these band gaps, mechanical waves decay exponentially and are thus mitigated. Phononic band gaps are formed through two main mechanisms, Bragg scattering and local resonance. Band gaps induced by Bragg scattering are dependent on order and the symmetry of the lattice and can be modified with a stronger or weaker mismatch in the mechanical impedance of a composite's materials [30,31]. Band gaps form by way of local resonance due to the excitation of resonant frequencies; these band gaps are independent of periodicity [32–37]. Phononic crystals with Bragg-type band gaps are limited, however, in their application because they do not attenuate vibration at lower frequencies without requiring large geometries. Inducing these lower frequency band gaps is being achieved through the production of phononic metamaterials that exploit locally resonant masses to absorb energy [38]. Despite these advances, the application of phononic metamaterials is largely hindered by their limited operation frequency ranges and inferior mechanical properties. Designing lightweight phononic metamaterials with low-frequency vibration mitigation capability is still challenging.

Here we choose architected hollow sphere foams (AHSFs) as the model system to address the above challenge. In the past decades, hollow sphere foams (HSFs) have been investigated intensively, because of their exceptional mechanical, thermal, and acoustic properties. For example, earlier finite element simulations have revealed that architected hollow sphere metallic foams with a face-centered cubic lattice symmetry exhibit the highest moduli and yield strength when compared with foams with other lattice symmetries [39,40]. In addition, anisotropic feature and considerable fatigue resistance of HSFs have been reported [41,42]. Under large deformation, HSFs show good energy absorption characteristic, which is controlled by loading rate, geometric parameters, and topologies [43]. These prominent mechanical properties make hollow sphere foams ideal candidate for automotive applications where lightweight design and enhanced mechanical properties are simultaneously pursued. In addition to these mechanical properties, theoretical models along with finite elements simulations indicate that architected hollow sphere foams can be designed with low thermal conductivity by tailoring the packing fraction, shell, and binder geometry [44]. In parallel, it has been demonstrated that both random and rationally designed HSFs can manipulate mechanical wave propagation. For instance, perforated HSFs with wide acoustic attenuation ranges show great promise to serve as acoustic liners for airplane engines [45]. Our recent numerical work further demonstrates that perforated AHSFs can simultaneously control sound and elastic wave propagation [46]. In addition to these multifunctionalities, HSFs offer manufacturing flexibility in material selection and can be assembled into relatively defect-free periodic structures [40,44], making them ideal for use in multiple fields of application. Because of the multifunctionalities, versatile design space, and manufacturing flexibility, AHSFs offer an ideal model system to investigate how to achieve lightweight phononic metamaterials with low-frequency vibration mitigation.

In this work, we designed and fabricated AHSFs composed of hollow spheres connected by binders with a body-centered-cubic (BCC) lattice symmetry (Fig. 1(a)). The unit cell for Bloch wave propagation analysis and detailed geometric description of each component can be found in Fig. 1(b) and (c). We demonstrate both experimentally and numerically the existence of phononic band gaps in the proposed AHSFs. Numerical simulations indicate that the band gap properties are controlled by the geometric features of the hollow sphere and binder. Remarkably, phononic band gap can be altered to a low-frequency range by tailoring the stiffness contrast between the hollow sphere and binder. In addition to the AHSF with a BCC lattice symmetry, we will show that the elastic wave phenomena persist in AHSFs with other topologies.

2. Wave propagation test and numerical model validation

We start by focusing on the existence of phononic band gaps in the proposed AHSFs through a combined experimental and numerical effort. For our simulations and experiment, the lattice constant of the unit cell is 3 cm and the volume fraction of the sample is 10.8%. The lattice constant is determined by the operating frequency range of the dynamic signal analyzer and the maximum build volume of our 3D printer. To avoid unsintered powder to be encapsulated inside the hollow spheres, AHSF model composed of $6 \times 3 \times 3$ unit cells was cut into six equivalent layers and fabricated by using an HP Jet Fusion 3D 4200 printer (Fig. 2(a)). Then, the six layers were glued together using glue gel, and the assembled sample was kept at room temperature for seven days to allow for the saturation of the curing. The mechanical properties of the constitutive material Nylon PA12 were measured by following ASTM D695. The basic properties of Nylon PA12 are characterized by Young's modulus $E = 1.312$ GPa, Poisson's ratio $\nu = 0.33$, and density of $\rho = 979\,\mathrm{kg\,m^{-3}}$.

To evaluate the vibration mitigation capability, elastic wave transmission tests were performed on the 3D printed AHSF, as shown in the experimental setup (Fig. 2(b)). An impact hammer with a hard tip (PCB Piezotronics, Model 086E80) was used to provide impulse forces exerted at the input end of the sample. To simulate the longitudinal polarization of the incident waves, we hit the left surface center of the sample along x-direction. The hammer can generate an impulse force with the frequency range up to 15 kHz that is sufficient to cover the frequency range of interest. To capture the longitudinally polarized wave signal transmitted from the input excitation, a piezoelectric accelerometer was attached to the right surface center of the sample using adhesive wax. To ensure that the hammer can hit the sample center and accelerometer can be attached well to the sample, we added two 3D printed patches ($3 \times 3 \times 0.1$ cm) on the left and right surfaces, respectively. A dynamic signal analyzer (Crystal Instrument corporation, COCO-80) was adopted to record both the input force and output acceleration. Fig. 2(c) shows the measured wave transmission spectrum, where a strong attenuation zone between 8.6 and 14.1 kHz can be observed.

To confirm the experimentally observed attenuation zone, we performed numerical simulations on the single unit cell and the finite size AHSF with $6 \times 1 \times 1$ unit cells using a commercial finite element package. Briefly, the phononic dispersion relation is constructed by performing eigenfrequency analyses to a unit cell, where Floquet-Bloch periodic boundary conditions are applied. The unit cell is discretized using 4-node tetrahedral elements, which are one-tenth of the minimum wavelength. The dynamic response of the proposed AHSF under elastic wave excitations is calculated by performing frequency domain analyses. Perfectly matched layers (PMLs) are applied at the two ends of the homogeneous parts to prevent reflections by scattering waves from the domain boundaries. More computational details on the eigenfrequency and frequency domain analyses can be found in our previous work [46,47]. Fig. 2(d) and (e) report the simulated phononic dispersion relation and transmission spectrum, respectively. Notably, we have a good qualitative agreement for the partial band gap between the simulations and experiments (highlighted in gray). The dynamic responses of the AHSF under harmonic excitation frequencies inside and outside the band gap further solidify this phenomenon (Fig. 2(f)). When the incident frequency lies outside the band gap (point A), elastic wave can propagate freely through the AHSF. By contrast, the incident wave energy will be reflected when the incident wave frequency is located inside the band gap (point B).

It should be noted that the attenuation zones in the measured transmission spectra are slightly shifted toward high frequencies. This discrepancy is due to the manufacturing defects in the thin walls of hollow spheres ($\sim$ 1 mm), including non-uniform wall thickness and voids among powder. These structural defects will not affect elastic wave propagation in the AHSF, since the wavelength is much larger

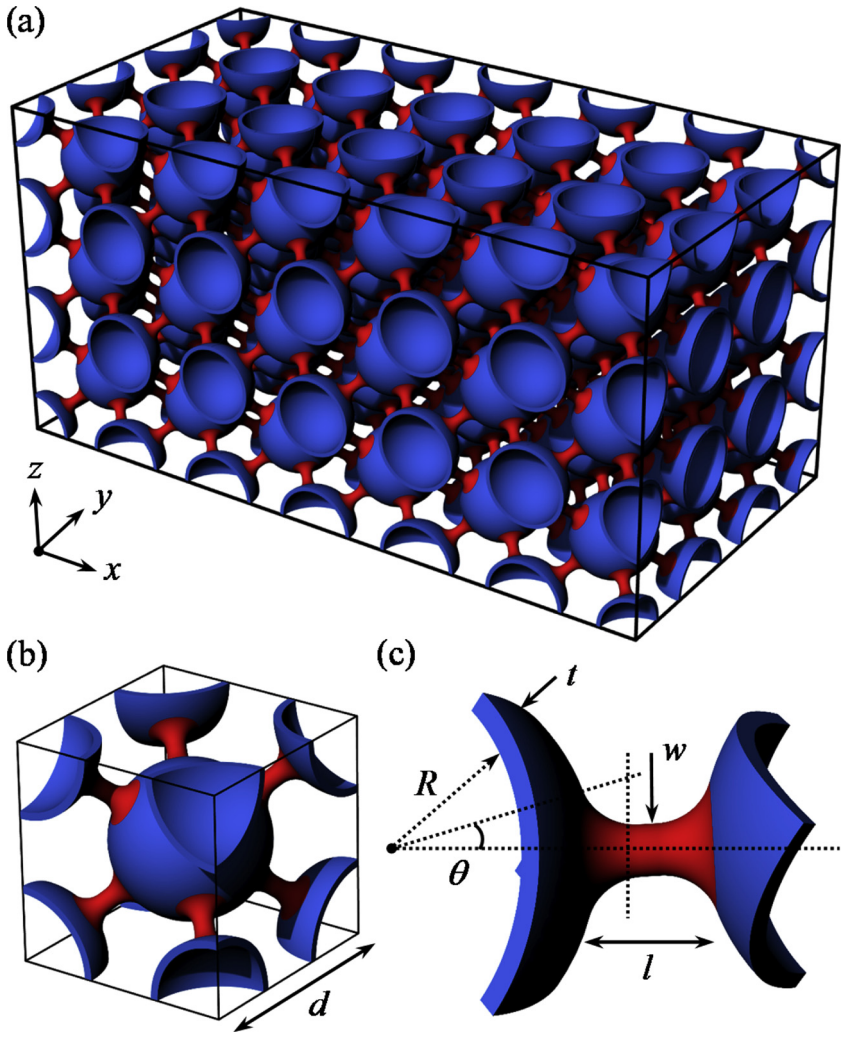

Fig. 1. Geometric description of the proposed architected hollow sphere foam (AHSF) with a body-centered-cubic (BCC) lattice symmetry. (a) AHSF consists of spheres (blue) and binders (red). (b) The unit cell of the AHSF for Bloch wave analysis. The lattice constant is d. (c) Dimensions of the hollow sphere and binder. Here R and t are the sphere's outer radius and thickness, respectively. l and w are the binder's length and diameter, respectively. θ is half of the angle subtended by the binder.

than the powder size. These defects, however, could affect the effective stiffness of the structure, which leads to the difference between the lower band gap boundary frequencies. In addition, intrinsic material damping affects mechanical wave attenuation at the high-frequency range, as one can see the attenuation from 14.1 kHz to 15 kHz. This attenuation zone is not attributed to the partial phononic band gap. Instead, inherent material damping of Nylon PA12 could be responsible for this. A detailed dynamic mechanical analysis is preferred to characterize the damping properties of this material but is not the focus of this study [48]. It should be pointed out the large difference between the transmission amplitude for experiment and simulation is due to the different model setups. Nevertheless, our dynamic tests evidence the existence of phononic band gap and thus wave attenuation capability of the proposed AHSFs. Since both the printing technique and wave transmission testing procedure are all well-established, in the rest of this work, we will only use numerical simulations to investigate the wave propagation phenomena in the AHSFs.

3. Design flexibility of phononic band gaps

3.1. Effect of geometric parameters

We then numerically investigate the effects of architected foam geometric features on the evolution of the first phononic band gap. The unique design of architected foams allows us to study the roles of the hollow sphere and binder independently. The mechanical properties of the constitutive material are defined by Young's modulus $E = 1.6$ GPa, Poisson's ratio $\nu = 0.33$, and density of $\rho = 1174\ \mathrm{kg\,m^{-3}}$ unless otherwise specified. As shown in Fig. 3(a), by increasing the fillet angle of binder, the relative size of the omnidirectional band gap decreases gradually. The relative band gap size was changed from 0.68 to 0.31 when the fillet angle is doubled from 10° to 20°. By contrast, the binder slenderness ratio has a pronounced impact on the band gap properties. For a wide binder ($l/w = 2$) representing a strong connection between binders and hollow spheres, the first omnidirectional band gap has a relatively small size of 0.1. When the binders become slender ($l/w = 10$) corresponding to a soft connection, the band gap size increases to 1.47, which is one order of magnitude larger (Fig. 3(b)). To further understand these trends, one can assume that the proposed AHSF behaves as a 3D mass-spring system, where hollow spheres act as lumped masses and binders work as springs. Each mass is accompanied by its eight nearest neighbors and connected by the spring. Analytical formulations reveal that the first omnidirectional phononic band gap results from oscillation and interaction among these masses [49–51] and thus the opening of the first band gaps are controlled by the geometric features of the binders and hollow spheres. To confirm this, Fig. 3(c) shows the

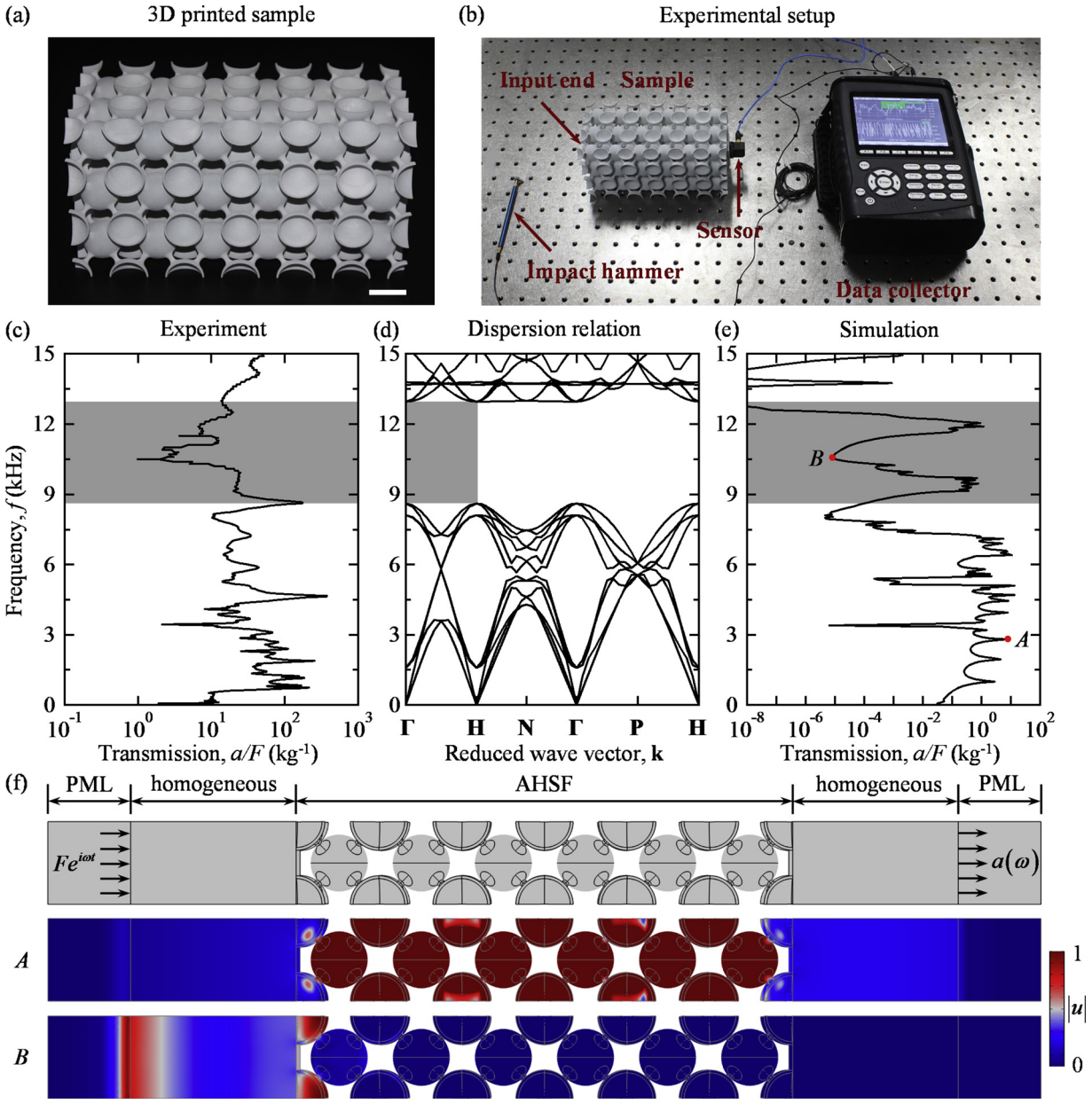

Fig. 2. Elastic wave transmission test on the 3D printed AHSF and numerical modeling validation. (a) 3D printed AHSF composed of 6 × 3 × 3 unit cells for elastic wave transmission test. Here $d = 3$ cm, $R = \sqrt{3}/5d$, $R/t = 10$, $l/w = 2$ and $\theta = 18°$. Scale bar: 2 cm. (b) Experimental setup for elastic wave propagation test. (c) Measured elastic wave transmission spectra along **ΓH** (x) direction. (d) Simulated phononic dispersion relation. (e) Simulated wave transmission spectrum. The gray shaded areas in (c)-(e) indicate the band gaps. (f) Finite element model and dynamic responses of the AHSF under excitation frequencies outside (point A: $f = 2.8$ kHz) and inside (point B: $f = 10.6$ kHz) the band gap. The color legend represents total displacement amplitude.

effect of hollow sphere thickness and thus the mass on the band gap properties. As expected, by increasing the sphere thickness and thus the lumped mass of the system, a larger omnidirectional band gap can be observed. These parametric analyses not only demonstrate the design flexibility of the proposed AHSFs with targeted phononic band gaps, but also imply that a weak connection among hollow spheres can lead to large band gap size in a low-frequency range.

3.2. Effect of stiffness contrast

We have shown the targeted phononic band gaps can be achieved by tailoring the geometric parameters of the AHSFs. Next, we fix the geometric parameters of the AHSFs and change the stiffness contrast between spheres and binders (E_s/E_b) to study the effect of this contrast on the band gaps. Here we choose $d = 3$ cm, $R = \sqrt{3}/5d$, $R/t = 10$, $l/w = 2$ and $\theta = 18°$. As displayed in Fig. 4, the first omnidirectional band gap is enlarged from $\Omega = 0.36 \sim 0.55$ to $\Omega = 0.18 \sim 0.53$ when the binder stiffness varies from one to one-tenth that of the sphere. By further decreasing the stiffness of the binders, the first band gap rapidly shifts toward a much lower frequency range. For example, when the stiffness ratio is $E_s/E_b = 1000$, the frequency range of the band gap decreases to $\Omega = 0.02 \sim 0.094$. To gain physical insights into this trend, we plot the eigenmodes at high symmetry points of the band edges, as shown in Fig. 4. The initial AHSF with a single constitutive material shows a Bragg type band gap because of the global vibration modes at the band edges (Fig. 4(a)–(b)). With the increase of stiffness contrast, the vibration modes demonstrate a strong localized characteristic. For example, as one can see in Fig. 4(c) and (d), the vibrational energy is localized in the hollow spheres at the upper band edges; at the lower band edges, the wave energy is concentrated on the soft binders.

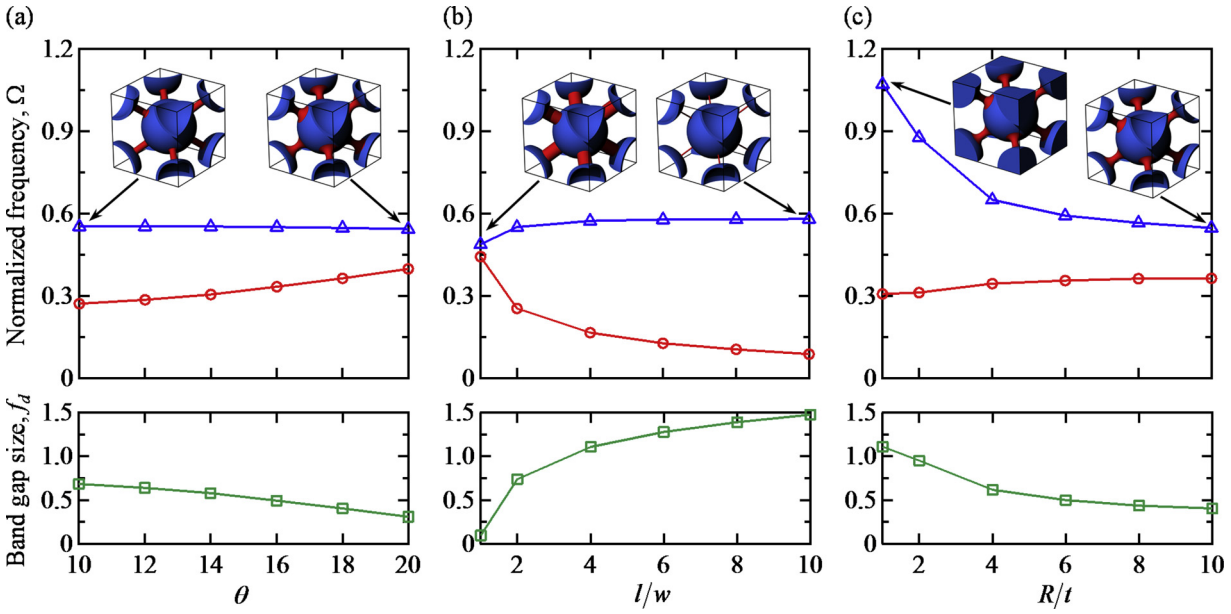

Fig. 3. Effects of binder and hollow sphere geometric features on the phononic band gap properties. (a) Effect of binder fillet angle. Here $d = 3$ cm, $R = \sqrt{3}/5d$, $R/t = 10$, and $l/w = 2$. (b) Effect of binder slenderness ratio. Here $d = 3$ cm, $R = \sqrt{3}/5d$, $R/t = 10$, and $\theta = 18°$. (c) Effect of hollow sphere thickness. Here $d = 3$ cm, $R = \sqrt{3}/5d$, $l/w = 2$, and $\theta = 18°$. The normalized frequency is defined as $\Omega = fd/c_t$, where c_t is the transverse velocity of the solid phase. The omnidirectional band gap size (green squares □) is defined as $f_d = 2(f_u - f_l)/(f_u + f_l)$, where f_u and f_l present the frequencies of upper (blue triangles **Δ**) and lower (red circles ○) band edge limits of the omnidirectional band gap, respectively.

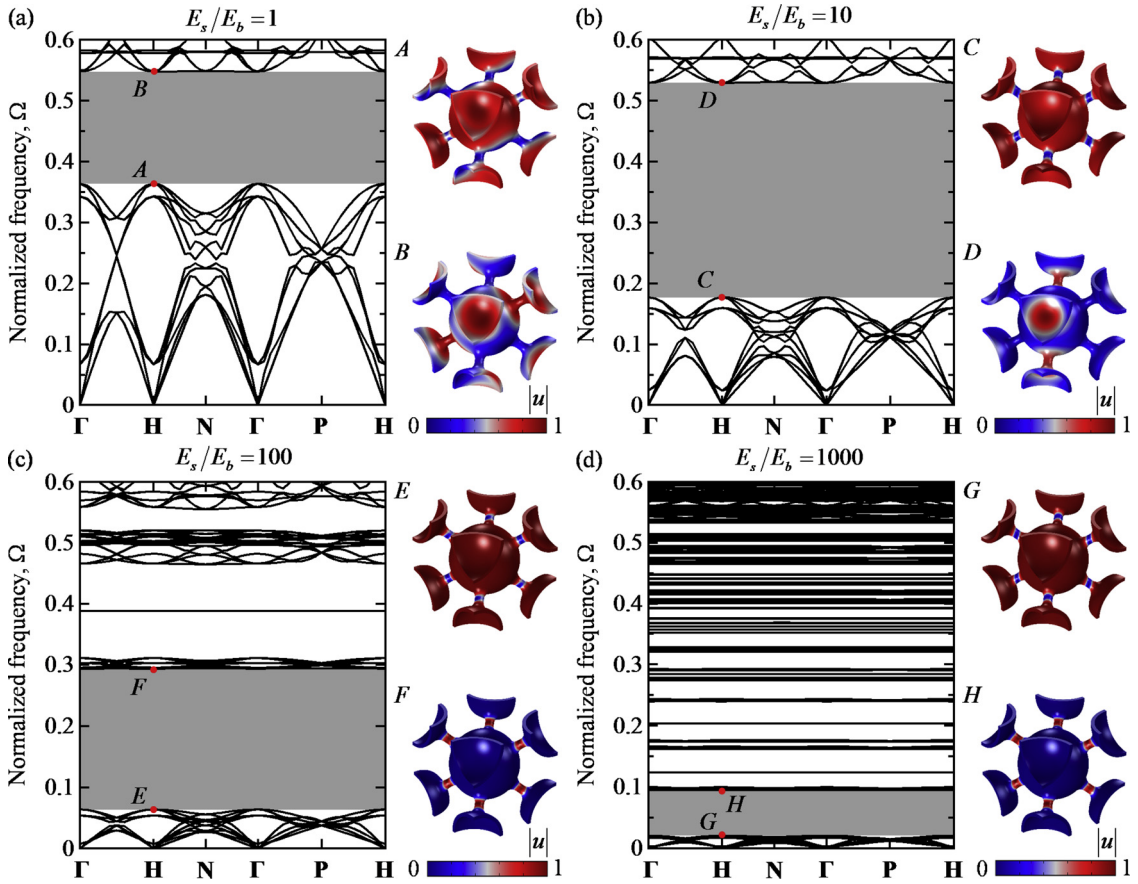

Fig. 4. Effect of stiffness contrasts between spheres (E_s) and binders (E_b) on phononic dispersion relations of the AHSF with a BCC lattice symmetry. (a) $E_s/E_b = 1$, (b) $E_s/E_b = 10$, (c) $E_s/E_b = 100$, and (d) $E_s/E_b = 1000$. Here $d = 3$ cm, $R = \sqrt{3}/5d$, $R/t = 10$, $l/w = 2$ and $\theta = 18°$. The gray shaded areas in the dispersion relations represent the first omnidirectional band gaps. The contour plots are eigenmodes at high symmetry points of the first irreducible Brillouin zone.

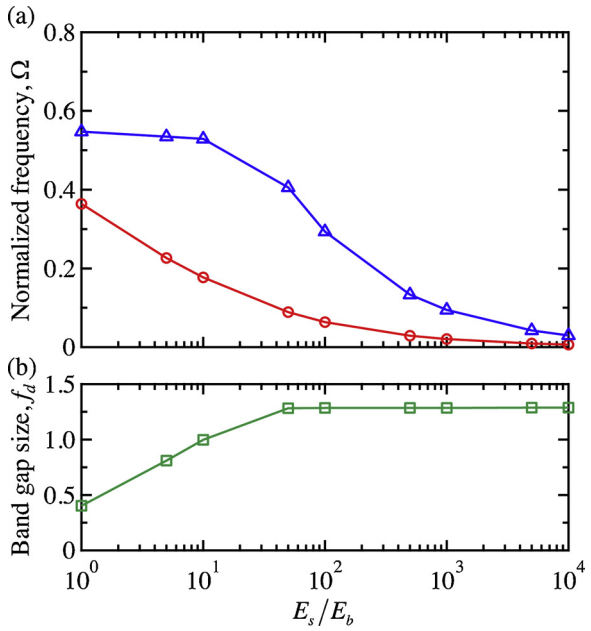

Fig. 5. Effect of stiffness contrast on the first phononic band gap properties. (a) Omnidirectional band gap position. (b) The relative band gap size of omnidirectional band gaps. For the definition of normalized frequency and band gap size, please refer to the caption of Fig. 3 for explanation.

Essentially, these eigenmodes analyses suggest that by tailoring the stiffness contrast between components, the band gap formation mechanisms can be switched from Bragg scattering to local resonance.

A more detailed analysis of the effect of stiffness contrast on the first band gap properties is summarized in Fig. 5. The band gap is abruptly shifted toward low-frequency range with the increase of stiffness ratio, while the relative band gap size increases linearly until a critical value is reached. At this threshold, the stiffness contrast is 50. Compared with conventional approaches such as harnessing structural instability to tune band gap properties [52–54], the proposed approach does not need to change the architectures by applying external stimuli. Importantly, compared with existing 3D phononic crystals [49,50,55–60], the proposed AHSF only requires a volume fraction of 10.8% while exhibiting a comparable band gap size exceeding 130%. This remarkable low-frequency band gap feature along with the lightweight design offers a promising approach for low-frequency vibration control, such as ground transportation induced vibrations and low amplitude seismic waves [47,61]. In addition to choose different constitutive materials, the stiffness contrast can be accomplished by using active materials, such as shape memory polymers [62], shape memory alloys [63], and magnetic elastomers [64,65]. As demonstrated by recent experimental work, the stiffness of 3D printed shape memory polymer can be tuned over three orders of magnitude by resistance wire heating [66]. For our case, by wrapping the binders with designed resistance wire, one can tune the binder stiffness and hence achieve tunable low-frequency band gaps, as predicted by our numerical simulations.

3.3. Effect of lattice symmetry

The elastic wave propagation results reported so far are focused on

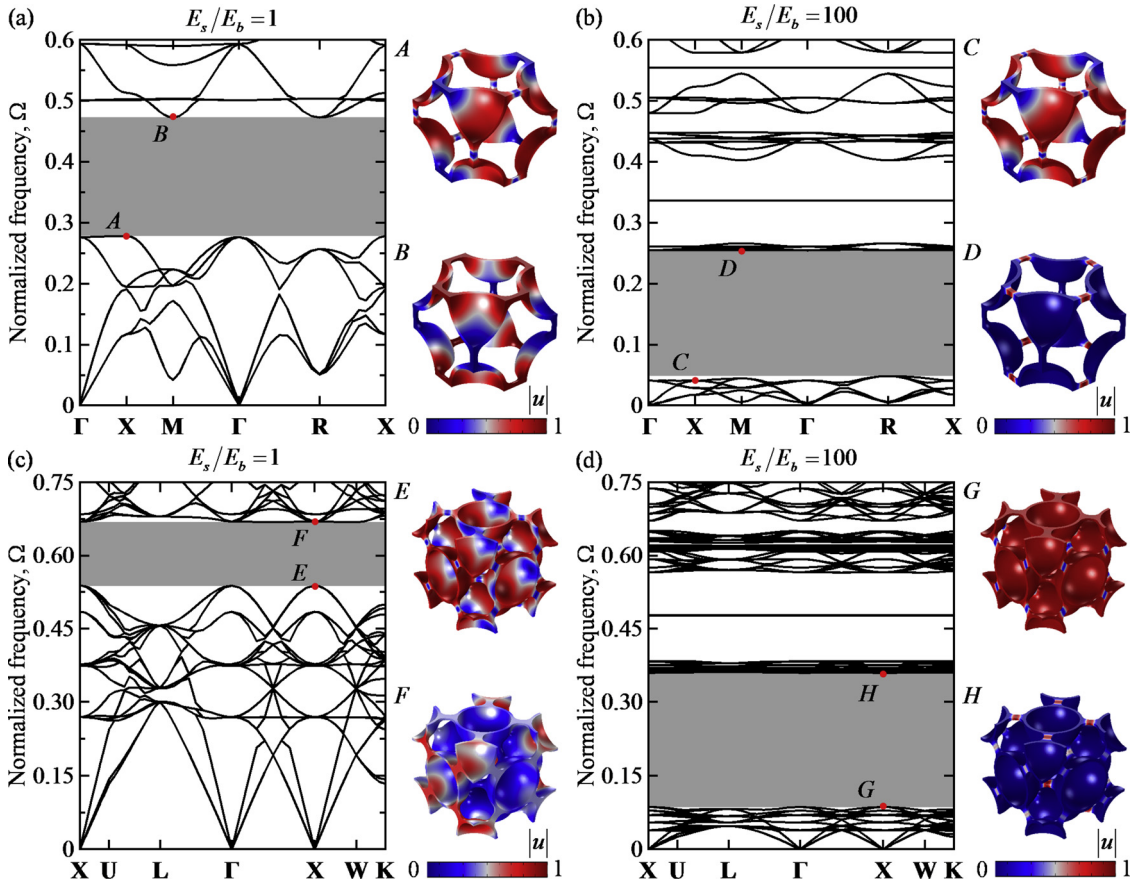

Fig. 6. Effect of lattice symmetry and stiffness contrast on phononic dispersion relations. (a)-(b) AHSFs with a simple cubic (SC) lattice symmetry, but with $E_s/E_b = 1$ and $E_s/E_b = 100$. (c)-(d) AHSFs with a face-centered-cubic (FCC) lattice symmetry, but with $E_s/E_b = 1$ and $E_s/E_b = 100$. Here $R = \sqrt{3}/5d$, $R/t = 10$, $l/w = 2$ and $\theta = 18°$.

AHSFs with a BCC lattice symmetry. We now proceed to examine the effect of lattice symmetry on the band gap properties. Fig. 6 reports the phononic dispersion relations of AHSFs with a simple cubic (SC) and a face-centered-cubic (FCC) lattice symmetry. For the AHSF with an SC lattice symmetry, an omnidirectional band gap is observed in $\Omega = 0.28 \sim 0.47$, which is shifted to $\Omega = 0.05 \sim 0.25$ when the stiffness contrast increases to 100. Notably, the relative band gap size is enlarged from 0.52 to 1.36. Similar evolution trend of the first band gap can be observed in the dispersion relations of the AHSF with an FCC lattice symmetry. The relative band gap size is increased from 0.22 to 1.23. Physically, the global vibration modes of the initial AHSFs with SC and FCC lattice symmetries indicate Bragg type band gaps, while the localized deformation patterns in AHSFs with a high stiffness contrast suggest locally resonant band gaps. These results imply that the proposed design strategy and physical mechanisms are robust and can be extended to architected foams with other topologies.

4. Conclusions

In summary, we have numerically and experimentally demonstrated the existence of an omnidirectional band gap in the 3D printed architected hollow sphere foam. The wave attenuation zone in the measured transmission spectrum agrees well with our our numerical predictions. Because of the unique design of the proposed architected foams, we have shown the design flexibility to change the band gap properties by tailoring the geometric and material parameters of the binder and hollow sphere. Remarkably, without changing the architecture or breaking lattice symmetry, the omnidirectional phononic band gaps can be shifted toward a low-frequency range by simply tailoring the stiffness contrast between hollow sphere and binder. We also evidenced that the proposed design paradigm and the physical mechanisms are robust and are applicable to AHSFs with other lattice symmetries. The findings reported in this work not only provide useful guidelines to design a new type of lightweight phononic metamaterials with low-frequency band gaps but also offers implications to develop active architected materials with tailored dynamic behaviors for a broad range of applications ranging from selective noise and vibration control to shock wave mitigation.

Author contributions

OM and HJ designed the models and performed numerical simulations, FQ conducted the wave transmission test, ZJ, LW, HM, and DC analyzed the data and discussed the results, YC and LZ supervised the research. All authors discussed the results and contributed to the final manuscript.

Declaration of Competing Interest

The authors declare no competing interests.

Acknowledgments

YC gratefully acknowledges the start-up fund from the Department of Mechanical Engineering at the University of Louisville. YC thanks Timothy Gornet (Rapid Prototyping Center, University of Louisville) for helping with the sample fabrication. YC thanks Dr. Kathryn Matlack (University of Illinois at Urbana-Champaign) for helpful discussion. LW acknowledges the partial support from the National Science Foundation (CMMI-1462270). The authors would like to thank the Editor and the anonymous Referees for the very constructive and useful comments.

References

[1] S.A. Stansfeld, M.P. Matheson, Noise pollution: non-auditory effects on health, Brit. Med. Bull. 68 (1) (2003) 243–257.
[2] M.G. Smith, I. Croy, M. Ögren, K.P. Waye, On the influence of freight trains on humans: a laboratory investigation of the impact of nocturnal low frequency vibration and noise on sleep and heart rate, PLoS One 8 (2) (2013) e55829.
[3] G.A. Athanasopoulos, P.C. Pelekis, Ground vibrations from sheetpile driving in urban environment: measurements, analysis and effects on buildings and occupants, Soil Dyn. Earthq. Eng. 19 (5) (2000) 371–387.
[4] W. Konon, J.R. Schuring, Vibration criteria for historic buildings, J. Constr. Eng. Manage. 111 (3) (1985) 208–215.
[5] E.I. Rivin, Vibration isolation of precision equipment, Precis. Eng. 17 (1) (1995) 41–56.
[6] L.L. Beranek, I.L. Ver, Noise and Vibration Control Engineering-principles and Applications, Wiley, 1992.
[7] S.M. Kuo, S. Mitra, W.-S. Gan, Active noise control system for headphone applications, IEEE Trans. Control Syst. Technol. 14 (2) (2006) 331–335.
[8] T.T. Soong, M.C. Costantinou, Passive and Active Structural Vibration Control in Civil Engineering, Springer, 2014.
[9] M. Basili, M. De Angelis, Optimal passive control of adjacent structures interconnected with nonlinear hysteretic devices, J. Sound Vib. 301 (1–2) (2007) 106–125.
[10] K.-M. Choi, H.-J. Jung, S.-W. Cho, I.-W. Lee, Application of smart passive damping system using MR damper to highway bridge structure, J. Mech. Sci. Technol. 21 (6) (2007) 870–874.
[11] S. Gasser, Y. Brechet, F. Paun, Materials design for acoustic liners: an example of tailored multifunctional materials, Adv. Eng. Mater. 6 (1–2) (2004) 97–102.
[12] S.U. Khan, C.Y. Li, N.A. Siddiqui, J.-K. Kim, Vibration damping characteristics of carbon fiber-reinforced composites containing multi-walled carbon nanotubes, Compos. Sci. Technol. 71 (12) (2011) 1486–1494.
[13] X. Huang, S. Zhou, G. Sun, G. Li, Y.M. Xie, Topology optimization for microstructures of viscoelastic composite materials, Comput. Methods Appl. Mech. Eng. 283 (2015) 503–516.
[14] A. Asadpoure, M. Tootkaboni, L. Valdevit, Topology optimization of multiphase architected materials for energy dissipation, Comput. Methods Appl. Mech. Eng. 325 (2017) 314–329.
[15] T.A. Schaedler, W.B. Carter, Architected cellular materials, Ann. Rev. Mater. Res. 46 (2016) 187–210.
[16] K. Bertoldi, Harnessing instabilities to design tunable architected cellular materials, Ann. Rev. Mater. Res. 47 (2017) 51–61.
[17] M.H. Lu, L. Feng, Y.F. Chen, Phononic crystals and acoustic metamaterials, Mater. Today 12 (12) (2009) 34–42.
[18] A. Khelif, B. Aoubiza, S. Mohammadi, A. Adibi, V. Laude, Complete band gaps in two-dimensional phononic crystal slabs, Phys. Rev. E 74 (4) (2006) 043509.
[19] J. Vasseur, P.A. Deymier, B. Chenni, B. Djafari-Rouhani, L. Dobrzynski, D. Prevost, Experimental and theoretical evidence for the existence of absolute acoustic band gaps in two-dimensional solid phononic crystals, Phys. Rev. Lett. 86 (14) (2001) 3012.
[20] M. Kushwaha, P. Halevi, Band-gap engineering in periodic elastic composites, Appl. Phys. Lett. 64 (9) (1994) 1085–1087.
[21] G. Zhang, X. Gao, Elastic wave propagation in a periodic composite plate structure: band gaps incorporating microstructure, surface energy and foundation effects, J. Mech. Mater. Struct. 14 (2) (2019) 219–236.
[22] G. Zhang, X.L. Gao, Elastic wave propagation in 3-D periodic composites: band gaps incorporating microstructure effects, Compos. Struct. 204 (2018) 920–932.
[23] W. Elmadih, W.P. Syam, I. Maskery, D. Chronopoulos, R. Leach, Mechanical vibration bandgaps in surface-based lattices, Addit. Manuf. 25 (2019) 421–429.
[24] T. Ampatzidis, R.K. Leach, C. Tuck, D. Chronopoulos, Band gap behaviour of optimal one-dimensional composite structures with an additive manufactured stiffener, Compos. Part B-Eng. 153 (2018) 26–35.
[25] B. Xia, G. Wang, S. Zheng, Robust edge states of planar phononic crystals beyond high-symmetry points of Brillouin zones, J. Mech. Phys. Solids 124 (2019) 471–488.
[26] P. Zhang, A.C. To, Broadband wave filtering of bioinspired hierarchical phononic crystal, Appl. Phys. Lett. 102 (12) (2013) 121910.
[27] R. Hu, C. Oskay, Nonlocal homogenization model for wave dispersion and attenuation in elastic and viscoelastic periodic layered media, J. Appl. Mech. 84 (3) (2017) 031003.
[28] A. Bacigalupo, L. Gambarotta, Dispersive wave propagation in two-dimensional rigid periodic blocky materials with elastic interfaces, J. Mech. Phys. Solids 102 (2017) 165–186.
[29] M. Miniaci, A. Krushynska, A.S. Gliozzi, N. Kherraz, F. Bosia, N.M. Pugno, Design and fabrication of bioinspired hierarchical dissipative elastic metamaterials, Phys. Rev. A 10 (2) (2018) 024012.
[30] Z. Liu, C. Chan, P. Sheng, Three-component elastic wave band-gap material, Phys. Rev. B 65 (16) (2002) 165116.
[31] Y. Achaoui, A. Khelif, S. Benchabane, L. Robert, V. Laude, Experimental observation of locally-resonant and Bragg band gaps for surface guided waves in a phononic crystal of pillars, Phys. Rev. B 83 (10) (2011) 104201.
[32] G. Wang, X. Wen, J. Wen, L. Shao, Y. Liu, Two-dimensional locally resonant phononic crystals with binary structures, Phys. Rev. Lett. 93 (15) (2004) 154302.
[33] J.C. Hsu, Local resonances-induced low-frequency band gaps in two-dimensional phononic crystal slabs with periodic stepped resonators, J. Phys. D. Appl. Phys. 44 (5) (2011) 055401.
[34] Z. Liu, X. Zhang, Y. Mao, Y. Zhu, Z. Yang, C.T. Chan, P. Sheng, Locally resonant sonic materials, Science 289 (5485) (2000) 1734–1736.
[35] Y. Chen, L. Wang, Periodic co-continuous acoustic metamaterials with overlapping locally resonant and Bragg band gaps, Appl. Phys. Lett. 105 (19) (2014) 191907.
[36] Y. Chen, L. Wang, Bio-inspired heterogeneous composites for broadband vibration mitigation, Sci. Rep. 5 (2015) 17865.

[37] A.O. Krushynska, V.G. Kouznetsova, M.G. Geers, Towards optimal design of locally resonant acoustic metamaterials, J. Mech. Phys. Solids 71 (2014) 179–196.
[38] K.H. Matlack, A. Bauhofer, S. Krödel, A. Palermo, C. Daraio, Composite 3D-printed metastructures for low-frequency and broadband vibration absorption, PNAS 113 (30) (2016) 8386–8390.
[39] W.S. Sanders, L.J. Gibson, Mechanics of BCC and FCC hollow-sphere foams, Mater. Sci. Eng. R 352 (1–2) (2003) 150–161.
[40] W.S. Sanders, L. Gibson, Mechanics of hollow sphere foams, Mater. Sci. Eng. R 347 (1–2) (2003) 70–85.
[41] O. Caty, E. Maire, R. Bouchet, Fatigue of metal hollow spheres structures, Adv. Eng. Mater. 10 (3) (2008) 179–184.
[42] T. Fiedler, A. Öchsner, On the anisotropy of adhesively bonded metallic hollow sphere structures, Scripta Mater. 58 (8) (2008) 695–698.
[43] A. Taşdemirci, Ç. Ergönenç, M. Güden, Split Hopkinson pressure bar multiple reloading and modeling of a 316 L stainless steel metallic hollow sphere structure, Int. J. Impact Eng. 37 (3) (2010) 250–259.
[44] Z. Jia, Z. Wang, D. Hwang, L. Wang, Prediction of the effective thermal conductivity of hollow sphere foams, ACS Appl. Energy Mater. 1 (3) (2018) 1146–1157.
[45] K. Ahuja, J. Gaeta, R.K. Ahuja, J. Gaeta, A new wide-band acoustic liner with high temperature capability, 3rd AIAA/CEAS Aeroacoustics Conference (1997) 1701.
[46] H. Jiang, Y. Chen, Lightweight architected hollow sphere foams for simultaneous noise and vibration control, J. Phys. D Appl. Phys. (2019).
[47] Y. Chen, F. Qian, F. Scarpa, L. Zuo, X. Zhuang, Harnessing multi-layered soil to design seismic metamaterials with ultralow frequency band gaps, Mater. Des. 175 (2019) 107813.
[48] A. Pérez-Peña, A.A. García-Granada, J. Menacho, J.J. Molins, G. Reyes, A methodology for damping measurement of engineering materials: application to a structure under bending and torsion loading, J. Vib. Control 22 (10) (2016) 2471–2481.
[49] F. Lucklum, M.J. Vellekoop, Bandgap engineering of three-dimensional phononic crystals in a simple cubic lattice, Appl. Phys. Lett. 113 (20) (2018) 201902.
[50] L. D'Alessandro, E. Belloni, R. Ardito, F. Braghin, A. Corigliano, Mechanical low-frequency filter via modes separation in 3D periodic structures, Appl. Phys. Lett. 111 (23) (2017) 231902.
[51] L. Brillouin, Wave Propagation in Periodic Structures: Electric Filters and Crystal Lattices, McGraw-Hill, 1946.
[52] P. Wang, F. Casadei, S. Shan, J.C. Weaver, K. Bertoldi, Harnessing buckling to design tunable locally resonant acoustic metamaterials, Phys. Rev. Lett. 113 (1) (2014) 014301.
[53] K. Bertoldi, M.C. Boyce, Mechanically triggered transformations of phononic band gaps in periodic elastomeric structures, Phys. Rev. B 77 (5) (2008) 052105.
[54] S. Rudykh, M.C. Boyce, Transforming wave propagation in layered media via instability-induced interfacial wrinkling, Phys. Rev. Lett. 112 (3) (2014) 034301.
[55] L. D'Alessandro, E. Belloni, R. Ardito, A. Corigliano, F. Braghin, Modeling and experimental verification of an ultra-wide bandgap in 3D phononic crystal, Appl. Phys. Lett. 109 (22) (2016) 221907.
[56] L. D'Alessandro, V. Zega, R. Ardito, A. Corigliano, 3D auxetic single material periodic structure with ultra-wide tunable bandgap, Sci. Rep. 8 (1) (2018) 2262.
[57] L. D'Alessandro, R. Ardito, F. Braghin, A. Corigliano, Low frequency 3D ultra-wide vibration attenuation via elastic metamaterial, Sci. Rep. 9 (1) (2019) 8039.
[58] Z. Jia, Y. Chen, H. Yang, L. Wang, Designing phononic crystals with wide and robust band gaps, Phys. Rev. Appl. 9 (4) (2018) 044021.
[59] F. Warmuth, M. Wormser, C. Körner, Single phase 3D phononic band gap material, Sci. Rep. 7 (1) (2017) 3843.
[60] J. Li, V. Slesarenko, S. Rudykh, Microscopic instabilities and elastic wave propagation in finitely deformed laminates with compressible hyperelastic phases, Eur. J. Mech. A-Solid. 73 (2019) 126–136.
[61] S. Brûlé, E.H. Javelaud, S. Enoch, S. Guenneau, Experiments on seismic metamaterials: molding surface waves, Phys. Rev. Lett. 112 (13) (2014) 133901.
[62] Y. Liu, K. Gall, M.L. Dunn, A.R. Greenberg, J. Diani, Thermomechanics of shape memory polymers: uniaxial experiments and constitutive modeling, Int. J. Plasticity 22 (2) (2006) 279–313.
[63] L.C. Brinson, One-dimensional constitutive behavior of shape memory alloys: thermomechanical derivation with non-constant material functions and redefined martensite internal variable, J. Intel. Mater. Syst. Struct. 4 (2) (1993) 229–242.
[64] J.M. Ginder, M.E. Nichols, L.D. Elie, S.M. Clark, Controllable-stiffness components based on magnetorheological elastomers, 7th Annual International Symposium on Smart Structures and Materials 3985 (2000).
[65] J.M. Ginder, M.E. Nichols, L.D. Elie, J.L. Tardiff, Magnetorheological elastomers: properties and applications, 1999 Symposium on Smart Structures and Materials 3675 (1999).
[66] Y. Li, Y. Shen, S. Cao, X. Zhang, Y. Meng, Thermally triggered tunable vibration mitigation in Hoberman spherical lattice metamaterials, Appl. Phys. Lett. 114 (19) (2019) 191904.